

Enhancing SDO/HMI images using deep learning

C. J. Díaz Baso^{1,2} and A. Asensio Ramos^{1,2}

¹ Instituto de Astrofísica de Canarias, C/Vía Láctea s/n, E-38205 La Laguna, Tenerife, Spain

² Departamento de Astrofísica, Universidad de La Laguna, E-38206 La Laguna, Tenerife, Spain

ABSTRACT

Context. The Helioseismic and Magnetic Imager (HMI) provides continuum images and magnetograms with a cadence better than one every minute. It has been continuously observing the Sun 24 hours a day for the past 7 years. The obvious trade-off between cadence and spatial resolution makes that HMI is not enough to analyze the smallest-scale events in the solar atmosphere.

Aims. Our aim is developing a new method to enhance HMI data, simultaneously deconvolving and superresolving images and magnetograms. The resulting images will mimick observations with a diffraction-limited telescope twice the diameter of HMI.

Methods. The method, that we term Enhance, is based on two deep fully convolutional neural networks that input patches of HMI observations and output deconvolved and superresolved data. The neural networks are trained on synthetic data obtained from simulations of the emergence of solar active regions.

Results. We have obtained deconvolved and superresolved HMI images. To solve this ill-defined problem with infinite solutions we have used a neural network approach to add prior information from the simulations. We test Enhance against Hinode data that has been degraded to a 28 cm diameter telescope showing very good consistency. The code is open sourced for the community.

Key words. Techniques: image processing, Sun: magnetic fields, Methods: data analysis

1. Introduction

Astronomical observations from Earth are always limited by the presence of the atmosphere, which strongly disturbs the images. An obvious (but expensive) solution to this problem is to place the telescopes in space, which produce observations without any (or limited) atmospheric aberrations. Although the observations obtained from space are not affected by atmospheric seeing, the optical properties of the instrument still limits the observations. The final quality is also limited by additional budgetary reasons.

In the case of near-diffraction limited observations, the point spread function (PSF) establishes the maximum allowed spatial resolution. The PSF typically contains two different contributions. The central core is usually dominated by the Airy diffraction pattern, a consequence of the finite aperture of the telescope (plus other perturbations on the pupil of the telescope like the spiders used to keep the secondary mirror in place). The tails of the PSF are usually dominated by uncontrolled sources of dispersed light inside the instrument, the so-called stray light. It is known that the central core limits the spatial resolution of the observations (the smallest feature that one can see in the image), while the tails reduce the contrast of the image (Danilovic et al. 2010). Moreover, it is important to note that knowing the PSF of any instrument is a very complicated task.

If the PSF is known with some precision, it is possible to apply inversion or deconvolution techniques to partially remove the perturbing effect of the telescope. The deconvolution is usually carried out with the Richardson-Lucy algorithm (Richardson 1972), a maximum-likelihood solution to the inversion problem. Single image deconvolution is usually a very ill-defined problem and some kind of regularization has to be imposed. Typically, early-stopping the RL algorithm leads to a decent output, damping the high spatial frequencies that appear in any deconvolution process. However, a maximum a-posteriori approach in which

some prior information about the image is introduced gives much better results.

Fortunately, spectroscopic and spectropolarimetric observations provide multi-image observations of a field-of-view (FOV) and the deconvolution process is much better defined. This has been tried recently with great success by van Noort (2012), who also introduced a strong regularization by assuming that the Stokes profiles in every pixel have to be explained with the emerging Stokes profiles from a relatively simple model atmosphere assuming local thermodynamical equilibrium. Another solution was provided by Ruiz Cobo & Asensio Ramos (2013), who assumed that the matrix built with the Stokes profiles for all observed pixels has very low rank. This method was later exploited by Quintero Noda et al. (2015) with good results. Another different approach was developed by Asensio Ramos & de la Cruz Rodríguez (2015), who applied the assumption of sparsity on the wavelet decomposition of the spatially variant physical properties in the observed FOV to carry out inversions and deconvolution simultaneously.

The Helioseismic and Magnetic Imager (HMI; Scherrer et al. 2012) onboard the Solar Dynamics Observatory (SDO; Pesnell et al. 2012) is a space-borne observatory that deploys full-disk images (plus a magnetogram and dopplergram) of the Sun every 45 s (or every 720 s for a better signal-to-noise ratio). The spatial resolution of these images is $\sim 1.1''$, with a sampling of $\sim 0.5''/\text{pix}$. In spite of the enormous advantage of having such a synoptic telescope, the spatial resolution is not enough to track many of the small-scale solar structures of interest.

In the process of pushing the technological advance, one would desirably prefer images with a better spatial resolution (perhaps $\times 2$) and compensated for the telescope PSF. Under the assumption of a linear theory of image formation, and writing images in lexicographic order (so that they are assumed to be sampled at a given resolution), the observed image can be written

arXiv:1706.02933v1 [astro-ph.SR] 9 Jun 2017

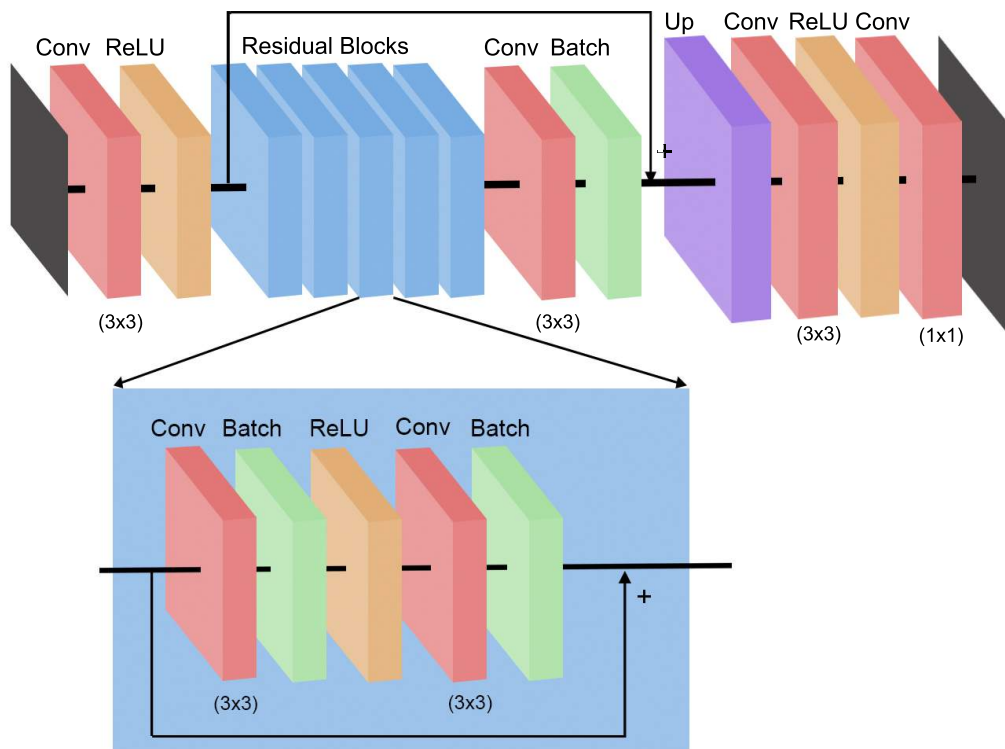


Fig. 1. Upper panel: architecture of the fully convolutional neural network used in this work. Lower panel: the inner structure of a residual block.

as:

$$\mathbf{i} = \mathbf{D}\mathbf{P}\mathbf{o} + \mathbf{e}, \quad (1)$$

where \mathbf{o} is the solar image at the entrance of the telescope, \mathbf{P} is a convolution matrix that applies the PSF to the image, \mathbf{D} is a sub-sampling matrix that reduces the resolution of the input image to the desired output spatial resolution and \mathbf{e} represents noise. The single-image deconvolution+superresolution problem is the recovery of \mathbf{o} (an image of $2N \times 2N$ pixels) from a single measurement \mathbf{i} (an image of $N \times N$ pixels). It is a very difficult problem, which typically has to be solved with maximum a-posteriori methods imposing priors (e.g., [Tipping & Bishop 2003](#)).

In spite of the difficulty of the problem, we think there is great interest in enhancing the HMI images using post-facto techniques. This motivated us to develop an end-to-end fast method based on a deep fully convolutional neural network that simultaneously deconvolve and superresolve by a factor of 2 the HMI continuum images and magnetograms. Deep learning single-image superresolution has been recently applied with great success in natural images ([Dong et al. 2015, 2016](#); [Shi et al. 2016](#); [Ledig et al. 2016](#)). Given the relatively small variability of solar structures (as compared with the variability of all possible natural images), a training-based approach gives much better results in our case than in the case of natural images. In the following, we give details about the architecture and training of the neural network and provide examples of applications to HMI data.

2. Method

2.1. Deep Neural Network topology

The deep neural networks (DNN) that we used in this work are inspired by that used by [Asensio Ramos et al. \(2017\)](#) to develop

DeepVel, used to measure horizontal velocity fields in the solar photosphere. Figure 1 shows the architecture. It is made of the concatenation of N residual blocks ([He et al. 2015](#)), that are marked in blue in the figure. The blowup shows the internal structure of each residual block. Each one is composed of several convolutional layers (two in our case) followed by batch normalizations ([Ioffe & Szegedy 2015](#)), and a rectified linear unit (ReLU [Nair & Hinton 2010](#)) activation for the first convolutional layer. There is also a shortcut connection between the input and the output of the block (see more information in [Asensio Ramos et al. 2017](#)), so that the input is plainly added to the output. This is a very smart way of accelerating training ([He et al. 2015](#)). All convolutions are carried out with kernels of size 3×3 and each convolutional layer uses 64 such kernels. Additionally, we also impose another shortcut connection between the input to the first residual block and the convolutional layer after the last residual block. We have checked that this slightly increase the quality of the prediction. Note that a convolution of an $M \times M$ image with a 3×3 kernel reduces the size of the output to $(M - 2) \times (M - 2)$. As usual, we augment the input image with 1 pixel in each side using a periodic padding to avoid this reduction and maintain the size of the input and output.

The main difference with the DNN of [Asensio Ramos et al. \(2017\)](#) is placed at the end, where we upsample the images to carry out the $\times 2$ superresolution. There are two main options to do superresolution with deep learning. The first involves upsampling the image just after the input and let the rest of convolutional layers do the work. The second involves doing the upsampling just before the output. Following [Dong et al. \(2016\)](#), we prefer the second option because it provides a much faster network, since the convolutions are applied to smaller images.

We build two deep neural networks like the ones described above, one to deconvolve and superresolve continuum images,

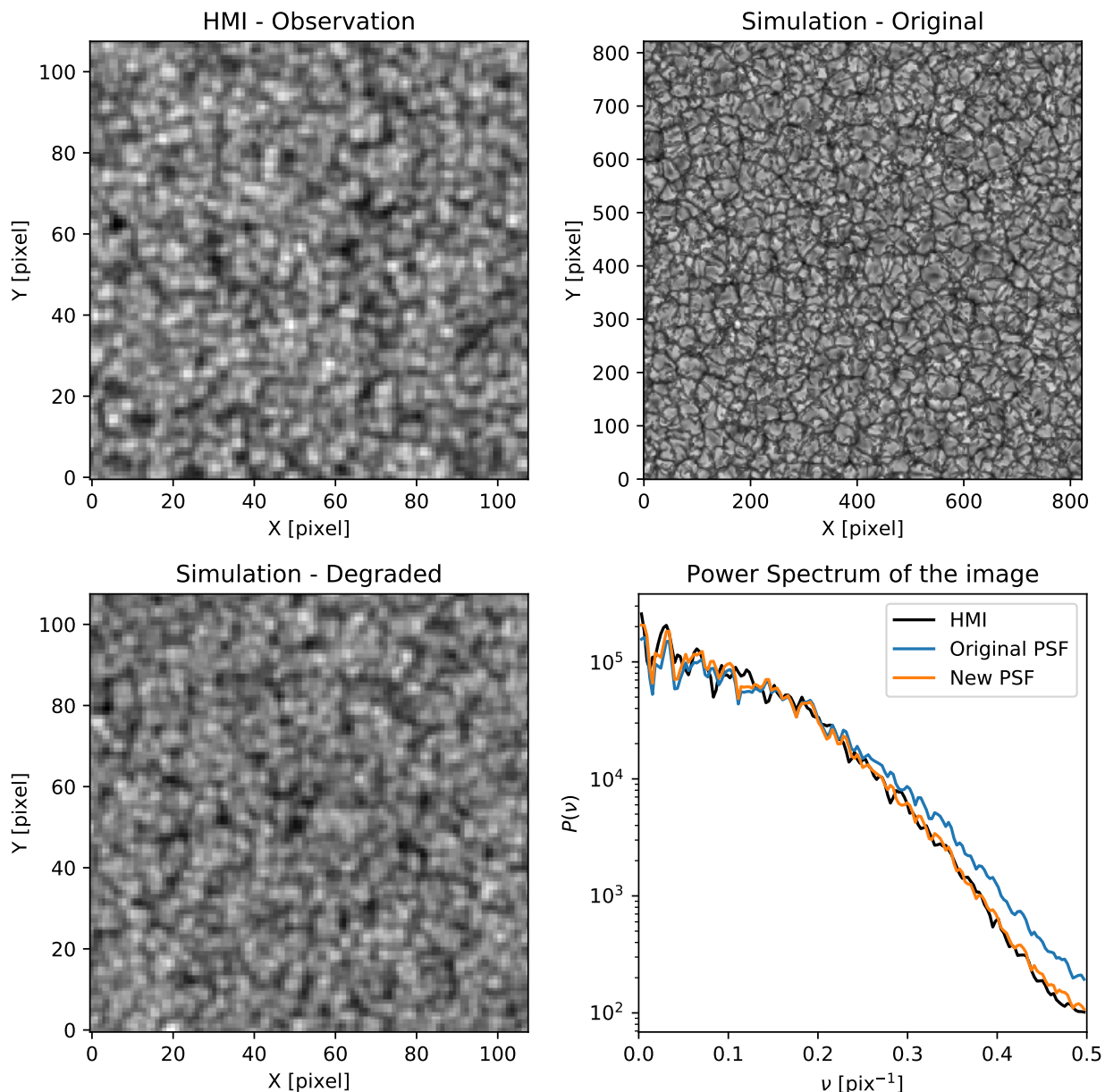


Fig. 2. Upper left: HMI observation. Upper right: snapshot from the simulation used for training. Lower left: degraded simulations, which can be compared with the HMI observations. Lower right: azimuthally averaged power spectrum of the HMI observations and the degraded simulations with the two considered PSFs.

and the other one for magnetograms. Although it could potentially be possible to use a single network both for continuum images and magnetograms, we have found much better results training two different networks. We refer to the set of two deep neural networks as Enhance.

2.2. Training data and training process

A crucial ingredient for the success of an DNN is the generation of a suitable training set of high quality. Our network is trained using synthetic continuum images and synthetic magnetograms from the simulation of the formation of a solar active region described by [Cheung et al. \(2010\)](#). This simulation provides a large FOV with many solar-like structures (quiet Sun, plage, umbra, penumbra, etc.) that visually resemble those in the real Sun. We note that if the DNN is trained properly and generalizes

well, the network does not memorize what is in the training set. On the contrary, it applies what it learns to the new structures. Therefore, we are not specially concerned by the potential lack of similarity between the solar structures in the simulation of [Cheung et al. \(2010\)](#) and the real Sun.

The radiative MHD simulation was carried out with the MU-RaM code ([Vögler et al. 2005](#)). The box spans $92 \text{ Mm} \times 49 \text{ Mm}$ in the two horizontal directions and 8.2 Mm in the vertical direction (with horizontal and vertical grid spacing of 48 and 32 km, respectively). After $\sim 20 \text{ h}$ of solar time, an active region is formed as a consequence of the buoyancy of an injected flux tube in the convection zone. An umbra, umbral dots, light bridges, and penumbral filaments are formed during the evolution. As commented before, this constitutes a very nice dataset of simulated images that look very similar to those on the Sun. Synthetic gray images are generated from the simulated snapshots ([Cheung et al.](#)

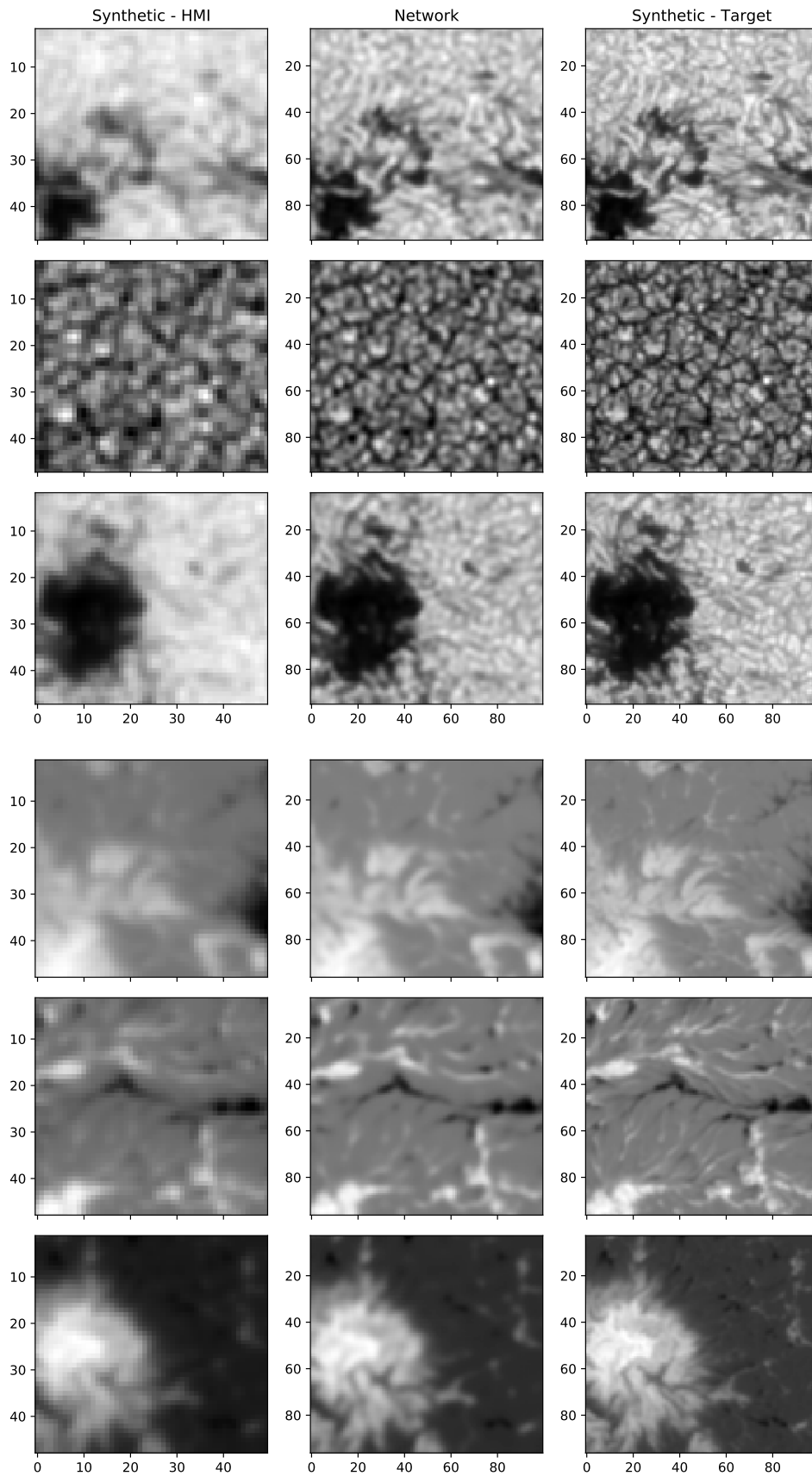


Fig. 3. Results with the synthetic validation set. The upper three rows show results for the continuum images, while the lower three rows display results for the magnetograms. All horizontal and vertical axes are in pixels.

2010) and magnetograms are obtained by just using the vertical magnetic field component at optical depth unity at 5000 Å. A total of 250 time steps are used in the training (slightly less for the magnetograms when the active region has already emerged to the surface).

The synthetic images (and magnetograms) are then treated to simulate a real HMI observation. All 250 frames of 1920×1024 images are convolved with the HMI PSF (Wachter et al. 2012; Yeo et al. 2014; Couvidat et al. 2016) and resampled to $0.504''/\text{pixel}$. For simplicity, we have used the PSF described in (Wachter et al. 2012). The PSF functional form is azimuthally symmetric and it is given by

$$\text{PSF}(r) = (1 - \epsilon) \exp \left[-\left(\frac{r}{\omega}\right)^2 \right] + \epsilon \left[1 + \left(\frac{r}{W}\right)^k \right]^{-1}, \quad (2)$$

which is a linear combination of a Gaussian and a Lorentzian. Note that the radial distance $r = \pi D \theta / \lambda$, with D the telescope diameter, λ the observing wavelength and θ the distance in the focal plane in arcsec. The reference values for the parameters (Wachter et al. 2012) are $\epsilon = 0.1$, $\omega = 1.8$, $k = 3$ and $W = 3$.

One could argue that using the more elaborate PSFs of Yeo et al. (2014) (obtained via observations of the Venus transit) or Couvidat et al. (2016) (obtained with ground data before the launch) is preferred. However, we point out that applying the PSF of Wachter et al. (2012) (with some modifications that are specified before) to the simulations produce images that compare excellently at a quantitative level with the observations. Anyway, given that our code is open sourced, anyone interested in using a different PSF can easily retrain the deep networks.

Then, we randomly extract 50000 patches of 50×50 pixels both spatially and temporally, which will constitute the input patches of the training set. We also randomly extract a smaller subset of 5000 patches which will act as a validation set to avoid overfitting. These are used during the training to check that the DNN generalizes well and is not memorizing the training set. The targets of the training set are obtained similarly but convolving with the Airy function of a telescope twice the diameter of HMI (28 cm), which gives a diffraction limit of $0.55''/\text{pixel}$, and then resampled to $0.25''/\text{pixel}$. Therefore, the sizes of the output patches are 100×100 . All inputs and outputs for the continuum images are normalized to the average intensity of the quiet Sun. This is very convenient when the network is deployed in production because this quantity is almost always available. On the contrary, the magnetograms are divided by 10^3 , so they are treated in kG during the training.

Figure 2 demonstrates the similarity between an HMI image of the quiet Sun (upper left panel) and the simulations degraded and downsampled (lower left panel). The simulation at the original resolution is displayed in the upper right panel. For clarity, we display the horizontal and vertical axis in pixel units, instead of physical units. This reveals the difference in spatial resolution, both from the PSF convolution and the resampling. We also realized that using the PSF of Wachter et al. (2012), the azimuthally averaged power spectrum of the degraded simulated quiet Sun turns out to have stronger tails than those of the observation. For this reason, we slightly modified it so that we use $\omega = 2$ and $W = 3.4$. For consistency, we also applied this PSF to the magneto-convection simulations described by Stein & Nordlund (2012) and Stein (2012), finding a similar improvement in the comparison with observations.

The training of the DNN is carried out by minimizing a loss function defined as the squared difference between the output of the network and the desired output defined on the training set.

To this end, we use the ADAM stochastic optimizer (Kingma & Ba 2014) with a learning rate of 10^{-4} . The training is done in a Titan X GPU for 20 epochs, taking ~ 500 seconds per epoch. We augment the loss function with an ℓ_2 regularization for the elements of the kernels of all convolutional layers to avoid overfitting. Finally, we add Gaussian noise (with an amplitude of 10^{-3} for the continuum images and 10^{-2} for the magnetograms) to stabilize the training and produce better quality predictions. This is important for regions of low contrast in the continuum images and regions of weak magnetic fields in the magnetograms.

There are a few hyperparameters that can be defined in the DNN. The most important ones are the number of kernels in each convolutional layer, their sizes, the number of residual blocks, the learning rate of the ADAM optimizer and the amount of regularization. We have found stable training behavior with a learning rate of 10^{-4} so we have kept this fixed. Likewise, using 64 kernels of 3×3 provide a very fast speed and good quality. Additionally, we found that a regularization weight of 10^{-6} for the continuum images and 10^{-5} for the magnetograms provides nice and stable results. Finally, five residual blocks provide predictions that are almost identical to those of 10 and 15 residual blocks but much faster. Therefore, we use $N = 5$.

3. Results

3.1. Validation with synthetic images

Before proceeding to applying the networks to real data, we show in Fig. 3 the results with some of the patches from the validation set which are not used during the training. The upper three rows show results for the continuum images, while the lower three rows show results for the magnetograms. The leftmost column is the original synthetic image at the resolution of HMI. The rightmost column is the target that should be recovered by the network, which has doubled the number of pixels in each dimension. The middle column displays our single-image superresolution results.

Even though the appearance of all small-scale details are not exactly similar to the target, we consider that Enhance is doing a very good job in deconvolving and superresolving the data in the first column. In the regions of increased activity, we find that we are able to greatly improve the fine structure, specially in the penumbra. Many details are barely visible in the synthetic HMI image but can be guessed. Of special relevance are the protrusions in the umbra in the third row, which are very well recovered by the neural network. The network also does a very good job in the quiet Sun, correctly recovering the shape of the granules from the blobby appearance in the HMI images.

3.2. In the wild

The trained networks are then applied to real HMI data. In order to validate the output of our neural network we have selected observations of the Broadband Filter Instrument (BFI) from the Solar Optical Telescope/FilterGram (SOT/FG; Ichimoto et al. 2008) onboard Hinode (Tsuneta et al. 2008). The pixel size of the BFI is $0.109''$ and the selected observations were obtained in the red continuum filter at $6684 \pm 2 \text{ \AA}$, which is the one closer to the observing wavelength of HMI. To properly compare our results with Hinode, we have convolved the BFI images with an Airy function of a telescope of 28 cm diameter and resampled to $0.25''/\text{pixel}$ to match those of the output of Enhance. The Hinode images have not been deconvolved from the influence of its PSF. We point out that the long tails of the Hinode PSF produce a

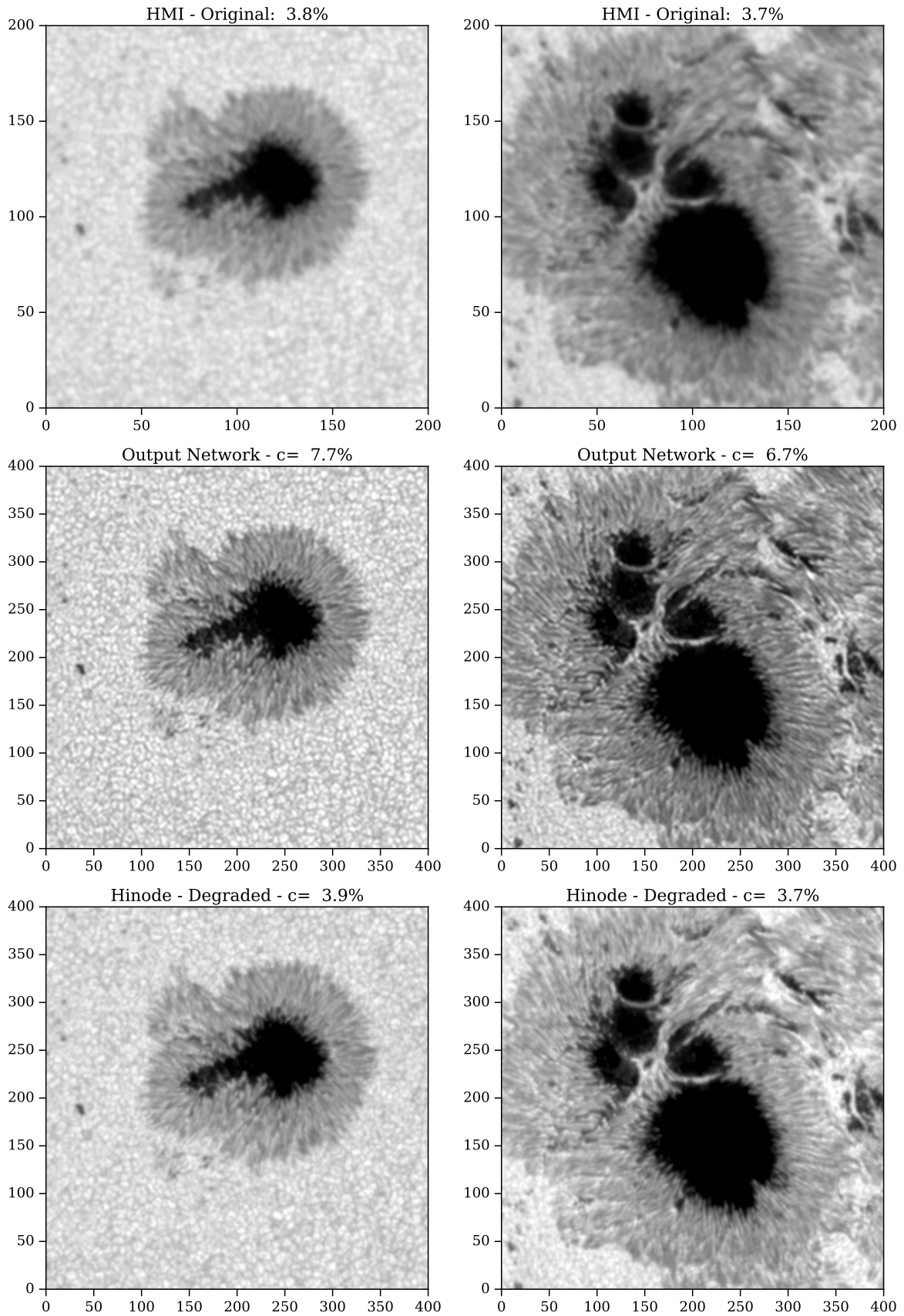


Fig. 4. This figure shows the application of the neural network to real HMI images. From the upper to the lower part of each column: the original HMI images, the output of the neural network and the degraded Hinode image. All the axis are in pixel units.

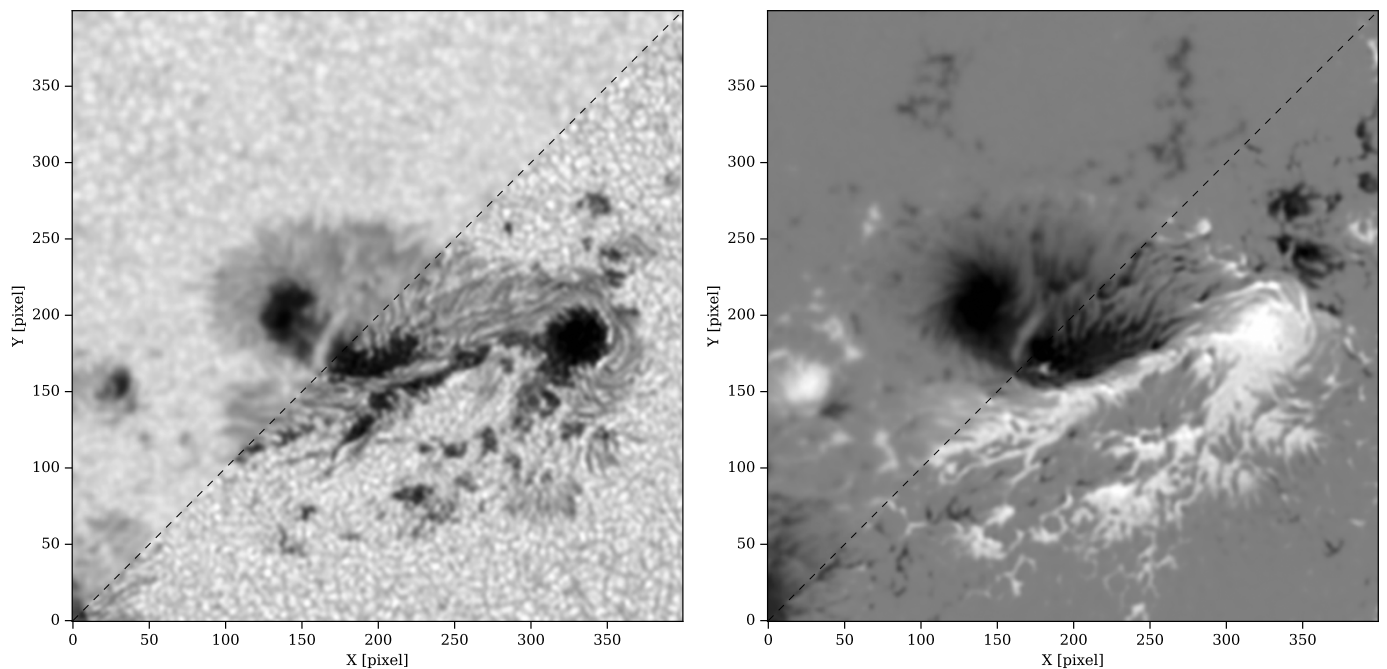


Fig. 5. This figure shows an example of our neural network applied to the intensity (left) and magnetogram (right) for the same region. The FOV is divided in two halves. The upper half shows the HMI original image, without applying the neural network. The lower half shows the enhanced image applying the neural network to the last image.

slight decrease of the contrast (Danilovic et al. 2010) and this is the reason why our enhanced images have a larger contrast.

3.2.1. Continuum images

Figure 4 displays this comparison for two different regions (columns) observed simultaneously with Hinode and HMI. These two active regions are: NOAA 11330 (N09, E04) observed on October 27, 2011 (first column) and NOAA 12192 (S14, E05) observed on October 22, 2014 (second column). We have used HMI images with a cadence of 45 seconds, which is the worst scenario in terms of noise in the image. The upper rows show the original HMI images. The lower rows display the degraded Hinode images, while the central row shows the output of our neural network. Given the fully convolutional character of the deep neural network used in this work, it can be applied seamlessly to input images of arbitrary size. As an example, an image of size 400×400 can be superresolved in ~ 100 ms seconds using a Titan X GPU, or ~ 1 s using a 3.4 GHz Intel Core i7.

The contrast quoted in the title of each panel has been obtained in a small region of the image displaying only granulation. The granulation contrast increases from $\sim 3.7\%$ to $\sim 7\%$ (as Couvidat et al. 2016), almost a factor 2 larger than the one provided by degraded Hinode. Note that the contrast may be slightly off for the right column because of the small quiet Sun area available. The granulation contrast measured in Hinode without degradation is around 7%. After the resampling, it goes down to the values quoted in the figure. We note that (Danilovic et al. 2008) analyzed the Hinode granulation contrast at 630 nm and concluded that it is consistent with those predicted by the simulations (in the range 14–15%) once the PSF is taken into account. Just from the visual point of view, it is clear that Enhance produces small-scale structures that are almost absent in the HMI images but clearly present in the Hinode images. Additionally, the deconvolved and

superresolved umbra intensity decreases between 3 and 7% when compared to the original HMI umbral intensity.

Interesting cases are the large light bridge in the images of the right column, that increases in spatial complexity. Another examples are the regions around the light bridge, that are plagued with small weak umbral dots that are evident in Hinode data but completely smeared out in HMI. For instance, the region connecting the light bridge at (125, 240) with the penumbra. Another similar instance of this enhancement occurs (375, 190), a pore with some umbral dots that are almost absent in the HMI images.

As a caveat, we warn the users that the predictions of the neural network in areas close to the limb is poorer than those at disk center. The reason is that the spatial contrast is very small so the neural network does not know how to reconstruct them, thus creating artifacts. We speculate that these artifacts could be slightly reduced if limb synthetic observations are included in the training set.

3.2.2. A magnetogram example: AR 11158

As a final example, we show in Fig. 5 an example of the neural network applied to the intensity and the magnetogram for the same region: the NOAA 11158 (S21, W28), observed on February 15, 2011. The FOV is divided in two halves. The upper parts show the HMI original image both for the continuum image (left panel) and the magnetogram (right panel). The lower parts display the enhanced images after applying the neural network.

After the deconvolution of the magnetogram, we find: i) regions with very nearby opposite polarities suffer from an apparent cancellation in HMI data that can be restored with Enhance, giving rise to an increase in the absolute value of the longitudinal field; and ii) regions far from magnetized areas do get contaminated by the surroundings in HMI, which are also compensated for with Enhance, returning smaller longitudinal fields. The left panel of Fig. 6 shows the density plot of the input vs. output

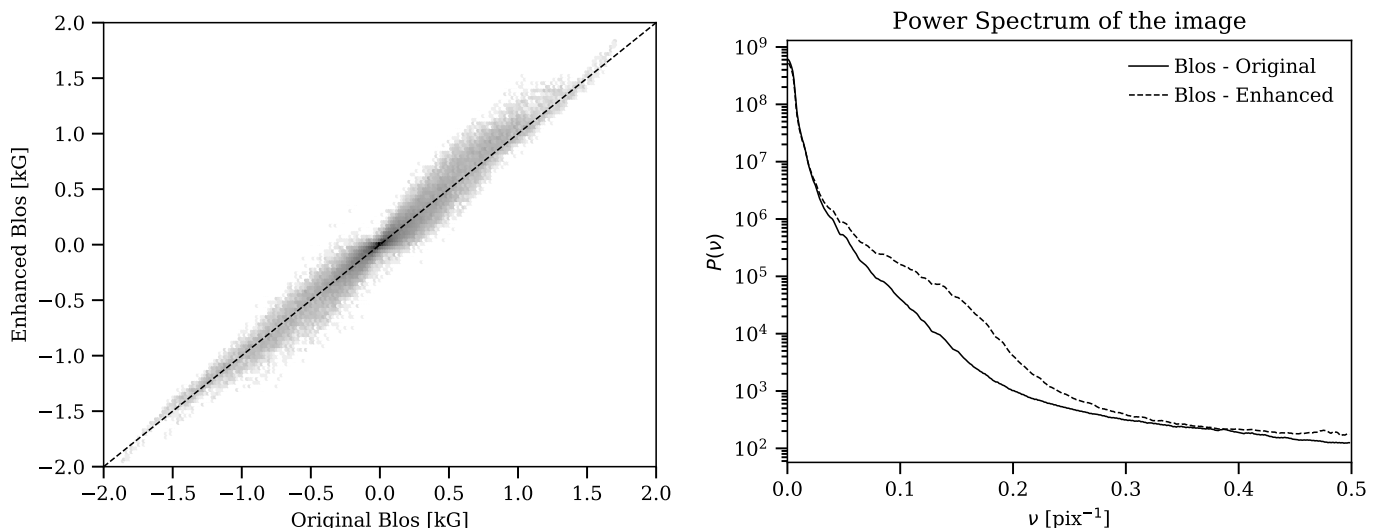


Fig. 6. Left: This figure shows the scatter plot between the original magnetogram and the deconvolved magnetogram. Right: This figure shows the power spectrum of each magnetogram: the original and the enhanced with the neural network.

longitudinal magnetic field. Almost all the points lie in the 1:1 relation. However, points around 1 kG for HMI are promoted to larger values in absolute value, a factor $\sim 1.3 - 1.4$ higher than the original image (Couvidat et al. 2016).

Another interesting point to study is the range of spatial scales at which Enhance is adding information. The right panel of Fig. 6 displays the power spectrum of both magnetograms showed in the right part of Fig. 5. The main difference between both curves is situated in the range of spatial scales $\nu = 0.05 - 0.25 \text{ pix}^{-1}$ with a peak at $\nu = 0.15 \text{ pix}^{-1}$. In other words, the neural network is operating mainly at scales between 4 and 20 pixels, where the smearing effect of the PSF is higher.

4. Conclusions and future work

This paper presents the first successful deconvolution and super-resolution applied on solar images using deep convolutional neural network. It represents, after Asensio Ramos et al. (2017), a new step toward the implementation of new machine learning techniques in the field of Solar Physics.

Single-image superresolution, either for continuum images or for magnetograms, is an ill-defined problem. It requires the addition of extra knowledge (a priori) for what to expect in the high-resolution images. The deep learning approach extracts this knowledge from the simulations and also applies a deconvolution. All this is done very fast, almost in real-time, and to images of arbitrary size. We hope that Enhance will allow researchers to study small-scale details in HMI images and magnetograms, something that cannot be currently done.

Often, HMI is used not as the primary source of information but as a complement for ground-based observations, providing the context. For this reason, having enhanced images where you can analyze the context with increased resolution is interesting.

We open-source Enhance¹, providing the methods to apply the trained networks used in this work to HMI images or re-train them using new data. In the future, we plan to extend the technique to other telescopes/instruments to generate superresolved and deconvolved images.

¹ <https://github.com/cdiazbas/enhance>

Acknowledgements. We thank Mark Cheung for kindly sharing with us the simulation data, without which this study would not have been possible. Financial support by the Spanish Ministry of Economy and Competitiveness through project AYA2014-60476-P is gratefully acknowledged. CJDB acknowledges Fundación La Caixa for the financial support received in the form of a PhD contract. We also thank the NVIDIA Corporation for the donation of the Titan X GPU used in this research. This research has made use of NASA's Astrophysics Data System Bibliographic Services. We acknowledge the community effort devoted to the development of the following open-source packages that were used in this work: numpy (numpy.org), matplotlib (matplotlib.org), Keras (keras.io), and Tensorflow tensorflow.org and SunPy sunpy.org.

References

- Asensio Ramos A., de la Cruz Rodríguez J., 2015, *A&A*, **577**, A140
 Asensio Ramos A., Requerey I. S., Vitas N., 2017, preprint, (arXiv:1703.05128)
 Cheung M. C. M., Rempel M., Title A. M., Schüssler M., 2010, *ApJ*, **720**, 233
 Couvidat S., et al., 2016, *Sol. Phys.*, **291**, 1887
 Danilovic S., Gandorfer A., Lagg A., Schüssler M., Solanki S. K., Vögler A., Katsukawa Y., Tsuneta S., 2008, *A&A*, **484**, L17
 Danilovic S., Schüssler M., Solanki S. K., 2010, *A&A*, **513**, A1
 Dong C., Change Loy C., He K., Tang X., 2015, preprint, (arXiv:1501.00092)
 Dong C., Change Loy C., Tang X., 2016, preprint, (arXiv:1608.00367)
 He K., Zhang X., Ren S., Sun J., 2015, preprint, (arXiv:1512.03385)
 Ichimoto K., et al., 2008, *Sol. Phys.*, **249**, 233
 Ioffe S., Szegedy C., 2015, in Blei D., Bach F., eds, Proceedings of the 32nd International Conference on Machine Learning (ICML-15). JMLR Workshop and Conference Proceedings, pp 448–456, <http://jmlr.org/proceedings/papers/v37/loffef15.pdf>
 Kingma D. P., Ba J., 2014, preprint, (arXiv:1412.6980)
 Ledig C., et al., 2016, preprint, (arXiv:1609.04802)
 Nair V., Hinton G. E., 2010, in Proceedings of the 27th International Conference on Machine Learning (ICML-10), June 21–24, 2010, Haifa, Israel. pp 807–814, <http://www.icml2010.org/papers/432.pdf>
 Pesnell W. D., Thompson B. J., Chamberlin P. C., 2012, *Sol. Phys.*, **275**, 3
 Quintero Noda C., Asensio Ramos A., Orozco Suárez D., Ruiz Cobo B., 2015, *A&A*, **579**, A3
 Richardson W. H., 1972, *Journal of the Optical Society of America* (1917–1983), **62**, 55
 Ruiz Cobo B., Asensio Ramos A., 2013, *A&A*, **549**, L4
 Scherrer P. H., et al., 2012, *Solar Physics*, **275**, 207
 Shi W., Caballero J., Huszar F., Totz J., Aitken A. P., Bishop R., Rueckert D., Wang Z., 2016, preprint, (arXiv:1609.05158)
 Stein R. F., 2012, *Living Reviews in Solar Physics*, **9**, 4
 Stein R. F., Nordlund A., 2012, *ApJ*, **753**, L13
 Tipping M. E., Bishop C. M., 2003, in *Advances in Neural Information Processing Systems*. MIT Press, pp 1303–1310
 Tsuneta S., et al., 2008, *Sol. Phys.*, **249**, 167

- Vögler A., Shelyag S., Schüssler M., Cattaneo F., Emonet T., Linde T., 2005, *A&A*, 429, 335
- Wachter R., Schou J., Rabello-Soares M. C., Miles J. W., Duvall T. L., Bush R. I., 2012, *Sol. Phys.*, 275, 261
- Yeo K. L., Feller A., Solanki S. K., Couvidat S., Danilovic S., Krivova N. A., 2014, *A&A*, 561, A22
- van Noort M., 2012, *A&A*, 548, A5